X-ray optics and beam characterization using random modulation: experiments

Sebastien Berujon,* Ruxandra Cojocaru, Pierre Piault, Rafael Celestre, Thomas Roth, Raymond Barrett and Eric Ziegler

European Synchrotron Radiation Facility, CS 40220, F-38043 Grenoble Cedex 9, France.
*Correspondence e-mail: xebastien@berujon.org

A parallel paper [Berujon, Cojocaru, Piault, Celestre, Roth, Barrett & Ziegler (2020), *J. Synchrotron Rad.* **27**, 284–292] reviewed theoretically some of the available processing schemes for X-ray wavefront sensing based on random modulation. Shown here are experimental applications of the technique for characterizing both refractive and reflective optical components. These fast and accurate X-ray at-wavelength metrology methods can assist the manufacture of X-ray optics that transport X-ray beams with a minimum amount of wavefront distortion. It is also recalled how such methods can facilitate online optimization of active optics.

1. Introduction

In our accompanying theoretical paper (Berujon *et al.*, 2020), we recalled the available X-ray near-field speckle-based methods for at-wavelength metrology and their associated processing schemes. These speckle-based methods make use of high-frequency wavefront intensity random modulations whose small features act as markers permitting the inference of the rays' trajectory. Since within the X-ray regime most of the available beams are only partially coherent at best, the observed X-ray speckle patterns do not actually fully develop as a result of an interference process but rather as the product of a mix of phase and amplitude modulation. The speckle generator needed to infer the phase distortion of the beam can be regarded as a random mask that has the possibility of moving perpendicular to the direction of the beam in order to provide additional or redundant information.

The speckle method, although numerically more sophisticated than other methods, can easily be implemented on a beamline. As a matter of fact, the method solely requires a speckle generator that is often very easy to source (*e.g.* a piece of sandpaper) and the distances involved are not very strict, permitting the quick and easy fitting of the technical apparatus on many beamlines. On the downside, to achieve an accuracy of the order of one nanoradian on the wavefront gradient, a (piezoelectric) nano-positioner is required.

The speckle-based methods are: X-ray speckle tracking (XST) (Bérujon *et al.*, 2012*b*), X-ray speckle vector tracking (XSVT) (Berujon & Ziegler, 2015), X-ray speckle scanning (XSS) (Berujon *et al.*, 2012*a*), and a hybrid processing scheme, less simple to implement, but also advantageous in several aspects. In the XST approach the beam phase is inferred using a dual-image correlation-based technique that enables single-pulse wavefront metrology (Berujon *et al.*, 2015). The other methods require micrometre-accurate scanning of a speckle generator object, eventually permitting one to achieve
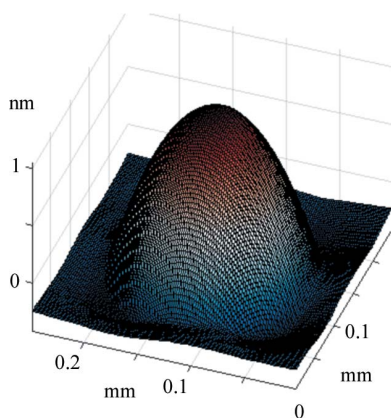
nanoradian sensitivity and pixel-size resolutions (Berujon & Ziegler, 2015).

In this paper we demonstrate the performances of the different speckle techniques by providing their corresponding implementations at a synchrotron beamline. We illustrate the potential of each method in a variety of at-wavelength metrology situations, using both refractive and reflective optics. The reader is referred to the first article of this dyad for more details regarding the numerical processing algorithms used herein (Berujon *et al.*, 2020).

At the ESRF, and more specifically at its Instrumentation Facility, beamline BM05 (Ziegler *et al.*, 2004), speckle-tracking methods are regularly applied for the at-wavelength characterization of new optical components and for development purposes. In this article, we present implementations of the previously presented near-field speckle schemes with experimental applications for beam, lens and mirror characterization.

Although the main focus of this work is on wavefront sensing and metrology for the characterization of X-ray optical components, one can envisage the applicability of the proposed methods to visible light optics, as suggested in recent work by Berto *et al.* (2017).

2. Experimental aspects

Although the requirements placed on the X-ray beam for the implementation of speckle-based techniques are rather minor, a couple of factors can induce systematic errors. One should try to minimize independently the errors induced by the beam, the detector and the speckle generator. In the following, we provide several recommendations to help the reader in achieving his or her own implementation of the techniques.

2.1. Data processing

The data presented here were processed using home-made routines coded in *MATLAB*. A non-supported version of some of these codes may be obtained from the authors upon request, whilst another more robust Python implementation is readily available at https://gitlab.esrf.fr/cojocaru/swarp, providing routines for the calculation of detector distortion and for wavefront analysis of the XST implementation schemes.

Beyond the code necessary for recovering the beam phase, mentioned above, additional processing routines must be integrated in order to extract additional information such as phase error or the thickness of a transmitting optic, or for a wavefront modal decomposition. As an example, see the processing steps for an X-ray lens at https://gitlab.esrf.fr/cojocaru.

2.2. Detector distortion

The detector can introduce systematic errors in the measurements. The main source of such errors is the distortion induced by the optical system used for recording high-reso-
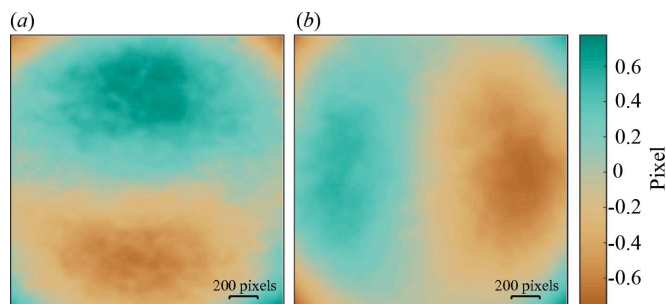
Figure 1
(*a*) Vertical and (*b*) horizontal detector distortions. The large stripe on the left corresponds to a mark on the Kapton window protecting the scintillator and is responsible for a local subpixel amplitude distortion.

lution images. For hard X-rays, high-resolution imaging detectors use a scintillator to convert the X-rays to visible light. The visible light image is then recorded by a digital camera through a magnifying optical system. The presence of lenses and a microscope objective are the main sources of image distortion. These systematic errors must be corrected for, as is also the case for grating-based methods (Inoue *et al.*, 2018).

We use the technique described by Berujon *et al.* (2015) to characterize the optical distortion of the imaging system at the beginning of each of our experiments using a 2D mesh scan of the detector positions perpendicular to the X-ray beam, consisting of 25 points placed on a square grid and located 20 µm apart. Fig. 1 displays the typical distortion of one of our X-ray imaging systems, consisting of a CMOS PCO Edge camera, a thin LSO:Tb scintillator of 10 µm thickness and magnifying optics that eventually lead to an effective pixel size of $p_{ix} = 0.615$ µm. In this case the peak-to-valley amplitude of the distortion is of the order of two pixels, but it can be much larger when employing detectors with larger chips and/or a microscope magnifying objective of lesser quality.

The calculated distortion is not used to correct all the recorded raw images but only the calculated gradient maps, using a two-dimensional bicubic interpolation. In the case of XSS, as the processing scheme operates pixel by pixel, no systematic errors from the detector are introduced in the angular measurement. In the other cases, where neighbouring pixels are included in the processing algorithm via a multi-pixel window function, the local detector distortion from one pixel to the neighbouring ones is so small ($<10^{-3}$ pixel per pixel) that its effect on the displacement vector is negligible. The only case where the raw images must be corrected is for the XST and XSVT methods used in absolute mode, since the same part of the beam will hit different areas of the detector for the two images. In such a case, the distortion between these two detector areas becomes a source of error for the calculation of the angular deflection generated by the phase gradient.

Further processing, like the fitting of polynomials to the calculated wavefront error, does require distortion correction because global (full detector frame) maps are considered in such an analysis.

2.3. Choice of a speckle generator material

The choice of the speckle generator material is not very restrictive and only a few practical guidelines can be given. One may want to test a few scattering objects empirically to find the one best suited for a certain experiment.

The criteria defining a good speckle generator object are the visibility of the speckle grains in the images and their size. In practice, the dimension of the grains should be selected so as to cover a few pixels of the image (<10 pixels) and with a minimum contrast of 0.1, where contrast can be defined as the standard deviation over the average intensity. Depending on the photon energy and the detector used, different choices can prove suitable, such as granular materials, sandpapers or filters (e.g. cellulose with micrometre pore sizes), used individually or in stacks. While the transverse coherence of the beam will help to increase the speckle contrast, the absorption of the material can also be used to generate speckle grains. In that case though, care should be taken to select a speckle membrane generator with an acceptable total absorption, that is stable in time, can handle the photon flux and does not diffract too much at larger scattering angles.

3. Metrology applications

The following metrology examples aim to demonstrate the validity of the speckle-based phase-sensing methods in various scenarios. As mentioned before, beyond the code necessary for phase retrieval from the speckle images, one should also consider subsequent analysis needs, usually involving the use of dedicated routines written specifically for optics metrology using an X-ray beam. For instance, the recovery of the shape error of a mirror requires the removal of the best surface, which depends on the design parameters of the reflective optics. In contrast, lens metrology will often call for polynomial wavefront decomposition in order to analyse the type of aberrations produced in the system. Such processing can represent a large part of the overall numerical treatment and may require user input, for example when defining the mask to be used when analysing a lens.

The metrology experiments presented here were conducted on beamline BM05 at the ESRF (Ziegler *et al.*, 2004). This beamline is a multipurpose facility equipped with a characterization platform devoted to the measurement of various optical components. The photons are produced by a 0.85 T dipole with electrons circulating in the ESRF storage ring with a nominal energy of $E = 6.03$ GeV. The X-ray spectrum accessible at the beamline is continuous and determined by the accelerator parameters. The critical photon energy of the bending magnet radiation is 19.2 keV.

3.1. Beam diagnostics

3.1.1. Absolute beam state. This first example aims to demonstrate the use of the XSVT method for the measurement of the absolute beam wavefront at a position of interest along the beamline.
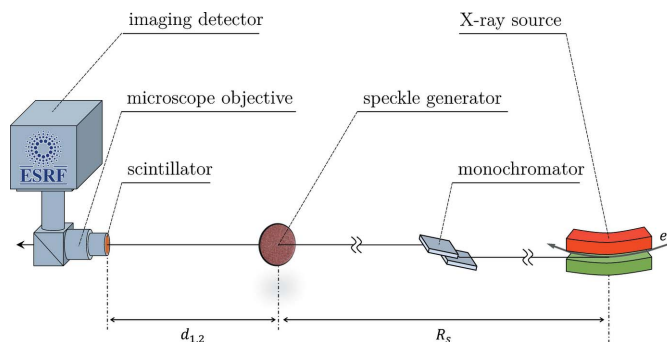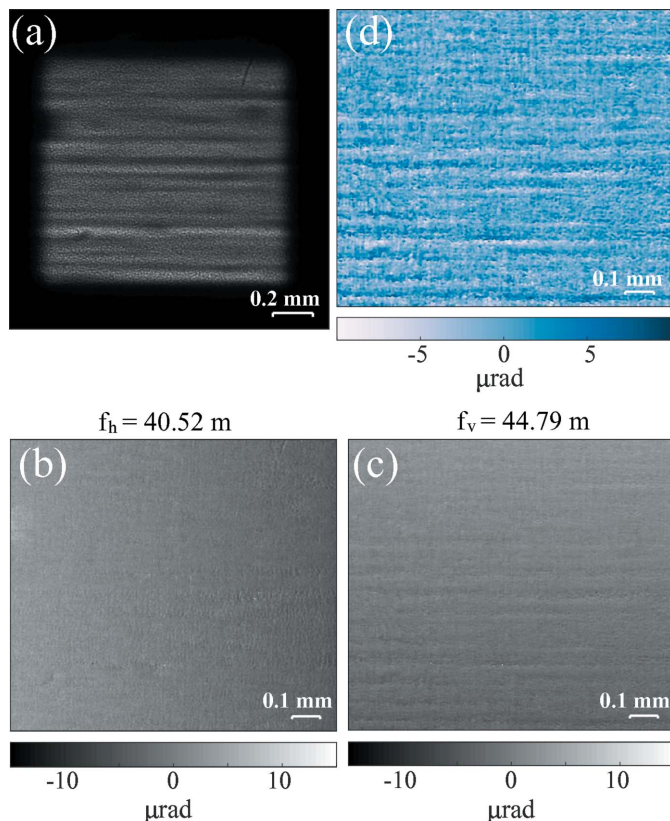

Figure 2
A sketch of the experimental configuration used to measure the X-ray wavefront state and stability of the ESRF BM05 beam after reflection on a double-crystal or multilayer monochromator.

The beam measured is that of BM05 when using a vertically deflecting multilayer monochromator with the energy set to $E = 17$ keV. The multilayer monochromator was designed with flat mirrors, preserving the natural divergence of the source upon reflection of the X-rays. The experimental configuration is sketched in Fig. 2, where the detector was moved along the beam axis between different data acquisitions. Two sets of 100 images at 100 well defined (but not equally spaced) transverse positions of the speckle membrane were collected sequentially in two propagation planes separated by $\Delta d = d_2 - d_1 = 200$ mm and located at approximately $R_S = 40.5$ m from the source. The detector was a FReLoN camera coupled to magnifying optics imaging a 10 µm thick LSO:Tb scintillator, rendering an effective pixel size of $p_{ix} = 0.78$ µm. Since XSVT has a sensitivity proportional to the detector pixel size, a high-resolution imaging detector is strongly recommended when implementing this technique in order to maximize its performance.

The XSVT approach was preferred here to the other methods, such as XSS in the self-correlation mode which could also have been an option. The XSS scheme presents the alternative advantage of not requiring the translation of the detector during the data collection, just that of the speckle generator. This can prove essential when experiment space on the beamline is limited. However, XSS also has some disadvantages that must be taken into account, like for instance its sensitivity to the local curvature of the beam. The use of XSS hence requires three separate steps of 2D numerical integration to reconstruct the beam's wavefront versus the single integration step required by XSVT. In our present case, the use of a high-resolution detector with XSVT helps us to gain angular resolution since it is proportional to the detector's pixel size.

Fig. 3(a) shows the speckles generated by the speckle membrane and the intensity fringes generated by the multilayer monochromator upon beam reflection. These are noticeable in the vertical wavefront gradient, shown in Fig. 3(c), and correspond to angular aberrations of the order of a few tens to hundreds of nanoradians as we shall see further on. An important parameter that can be extracted from this metrology is the slight astigmatism of the beam.

$f_h = 40.52$ m $f_v = 44.79$ m

Figure 3
The absolute wavefront as measured with speckle vector tracking. (a) First raw image. (b) and (c) Horizontal and vertical wavefront gradients. These gradients are compatible with a curved wavefront generated $f_h = 40.5$ m or $f_v = 44.8$ m away. (d) Vertical wavefront gradient error.

While in the horizontal direction (transverse to the monochromator double-bounce reflection in the vertical direction) the extracted source distance perfectly matches the physical distance from the source to the detector, a discrepancy is observed in the vertical direction. The calculated virtual vertical source distance is $f_v = 44.8$ m, compared with an expected value of $f = 40$ m. This aberration is introduced by the monochromator, perhaps due to surface errors of the mirrors or possibly due to a thermal bump generated on the first of these monochromator mirrors.

3.1.2. Beam stability measurements. The beam stability of a beamline can be monitored with XST, using sequences of images recorded with a fast time-sampling resolution. XST offers a good alternative for stability measurements since only a single image is needed to compare with a reference one, the method thus allowing dynamic processes to be tracked.

The example presented is again for beamline BM05 after monochromatization at $E = 17$ keV using the beamline's double-crystal Si(111) monochromator, using the same setup presented in Fig. 2.

In this experiment, the achievable time resolution limit is fixed by the X-ray flux density and by the minimum number of counts necessary on the detector for reliable tracking. The setup consisted solely of the static speckle generator and a PCO Edge 4.2 camera continuously acquiring images of the beam with an exposure time of 0.0125 s per frame (80 Hz).
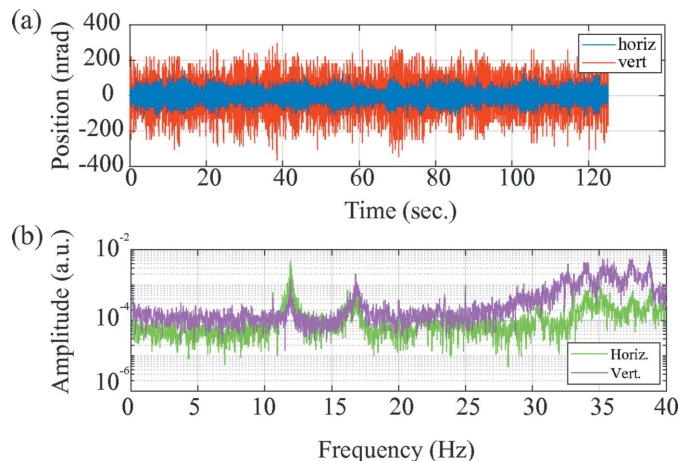
Figure 4
(a) The angular position of the beam tracked from image to image using the XST method. (b) Frequency decomposition showing the vibration modes.

The indirect magnifying optics (the X-ray image being converted to visible light through an LSO:Tb scintillator) led to an effective pixel size $p_{ix} = 1.6$ μm. The distance from the speckle generator to the detector was $d = 840$ mm, and $R_S = 40.5$ m remained unchanged.

Fig. 4(a) shows the measured angular positions of the beam as obtained by tracking the same large subset of pixels – and thus the speckles contained in it – across all the images collected over time. The angular positions are centred around the average position of the beam. Fig. 4(b) presents the time spectral decomposition of the angular beam positions. From these graphs, one can identify vibration modes, already known at the ESRF, at around 35 Hz and also peaks near 12 and 18 Hz originating from flow-induced vibrations coming from the monochromator cooling system. This application illustrates the potential of the method for beamline optimization and design.

The use of the XST-based method for monitoring beam stability presents the advantage of being much more photon efficient than alternative approaches that use a pinhole or focusing optics. Indeed, there is no or very little absorption in the monitoring device and many pixels are used to track the angular direction of the beam, whilst only a few pixels are used with the previously mentioned competing methods. The improved photon statistics offer a better performance in terms of noise and sensitivity. Moreover, the XST method can easily be applied at higher energies where the pinhole- and optics-based methods become challenging to implement.

3.2. Reflective optics

3.2.1. 2D mirror surface characterization. Online mirror metrology using the XSS technique was demonstrated by Berujon *et al.* (2014). A simplified and truncated 2D approach of the technique was later published by Wang *et al.* (2015) which can be effective for flat mirrors. In the following we demonstrate a more exact way of recovering the mirror shape for a strongly focusing mirror from 2D mesh scans of the
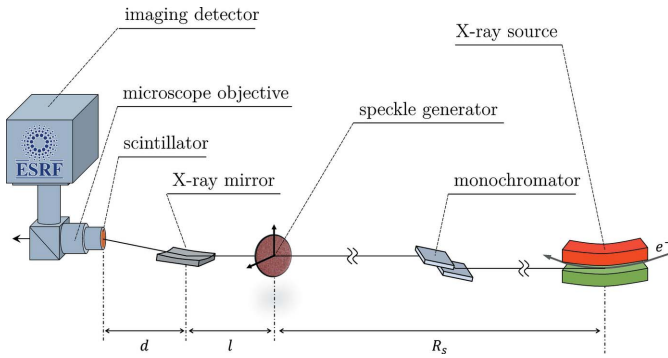
Figure 5
The setup used for the reflective optics characterizations.

speckle generator using the 2D absolute XSS method with self-correlation [see Section 2.2.5 of the theoretical paper, Berujon *et al.* (2020)].

The XSS approach revealed very early on its efficiency for the characterization of reflective optics (Berujon, 2013). Indeed, when measuring strongly focusing X-ray optics, the magnification generated by the investigated mirror (or alternatively by a lens, as seen in Section 3.3.2) permits the use of smaller speckle generator steps since they are enlarged by propagation and become discernible on the detector. That leads to the detection of smaller displacement vectors, thus achieving a higher accuracy in the method [see Fig. 4 in the paper by Berujon *et al.* (2020)]. Combined with a propagation distance d of several metres, the ultimate angular resolution can reach the order of a single nanoradian.

The experimental setup used corresponds to that shown in Fig. 5, where the camera is kept fixed during the 2D mesh scan of the speckle generator. The method applied here was a direct and complete application of the method described by Berujon *et al.* (2014) in two dimensions, which implies in practice a quadratic level of complexity: 4D data from XSS are used to obtain four curvature fields that are then iteratively integrated to obtain the 2D surface profile (Berujon & Ziegler, 2012a).

In more detail, from a 2D scan of the diffuser, four curvature fields of the wavefront W are obtained by applying the formulae of XSS in a self-correlation mode. Using the notation $\mathbf{r}$ for the transverse position of a pixel on the detector [*i.e.* on the basis of $(\mathbf{x}, \mathbf{y})$ transverse to the beam] and with N being an integer, we note $\Delta\mathbf{r}_x = N_{\text{pix}} \cdot \mathbf{x}$ or $\Delta\mathbf{r}_y = N_{\text{pix}} \cdot \mathbf{y}$ for the distance between two pixels located on the same row or column of the detector, respectively. Thus, we correlate the speckle signals of pixels with the signals received in the upper and lateral neighbouring pixels located at $\mathbf{r} + \Delta\mathbf{r}$ in order to find the corresponding signals' displacement vector $\upsilon_{x, y}$. Each cross-correlation operation provides two curvature fields κ_{ij} with $i, j \in [x, y]$ in the orthogonal reference $(\mathbf{x}, \mathbf{y})$ coming from the relationship

$$R_{ij}^{-1} = \kappa_{ij} = \frac{(1 - \upsilon_j/\Delta\mathbf{r}_i)}{d}, \tag{1}$$

derived from the local magnification defining $\Delta\mathbf{r}/\upsilon = R/(R - d - l)$ [see Section 2.2.5 in the paper by Berujon *et al.* (2020)], with R being the wavefront curvature radius,

$$\kappa_{xx} = \frac{\partial^2 W}{\partial x^2}, \quad \kappa_{xy} = \frac{\partial^2 W}{\partial y \partial x},$$
$$\kappa_{yy} = \frac{\partial^2 W}{\partial y^2}, \quad \kappa_{yx} = \frac{\partial^2 W}{\partial x \partial y}, \tag{2}$$

from which the two wavefront gradients, $\partial W/\partial x$ and $\partial W/\partial y$, are recovered through a 2D numerical integration method (Frankot & Chellappa, 1988; Southwell, 1980; Noll, 1978; Arnison *et al.*, 2004; Berujon *et al.*, 2015). Finally, a third 2D integration of $\partial W/\partial x$ and $\partial W/\partial y$ provides W. For an X-ray mirror with a sag of a few micrometres and when working at shallow angles, it was shown that an iterative corrective approach must be employed for an accurate surface mapping (Berujon & Ziegler, 2012b). For the present 2D approach, this iterative procedure necessarily imposes the recovery of the four curvature fields, a condition not fulfilled in the work of Wang *et al.* (2015).

Figs. 6(a)–6(d) show the four curvature fields obtained using XSS in self-correlation mode for the 2D characterization of the Zeiss substrate used by Berujon & Ziegler (2012b). The optical surface is 50 mm long, the incidence angle of the measurement was 0.13°, $l \simeq 400$ mm and $d = 1034$ mm. The speckle generator mesh scan comprised 32×32 points. In this example, the step sizes used for the scan of the membrane were different for the horizontal and vertical directions, with respective values of 0.25 µm and 2.9 µm (half the size of a pixel since there is no magnification in that direction). In the processing, we used $\Delta\mathbf{r} = 4p_{\text{ix}}$, which has a value clearly larger than that of the detector point spread function, but is still small enough to preserve the resolution provided by the detector. The FReLoN camera coupled to its optics gave an effective pixel size of $p_{\text{ix}} = 5.8$ µm. The magnification of the X-ray optics was then used to increase the angular sensitivity $\delta\alpha \propto \delta\tau$ through the factor Γ [since a good choice of speckle generator step is $\delta\tau \simeq p_{\text{ix}}/\Gamma$, *cf* Berujon *et al.* (2020)] and the sampling resolution on the mirror in the longitudinal direction. Fig. 6(f) is a 3D rendering of the mirror's tangential slope error from the targeted ellipse.

3.2.2. Multilayer interference fringes. We illustrate the use of the previous methods for this case, which is restricted to a single dimension, providing yet another investigative application. A problem often encountered when using reflective optics, either in total reflection or with reflective multilayer coatings, is the appearance in the reflected beam of intensity fringes oriented perpendicular to the photon propagation direction and orthogonal to the reflection normal axis. These fringes can be detrimental for many applications such as imaging, where they hinder the full use of the dynamic range of the detectors, and may complicate intensity normalization processing.

According to Morawe *et al.* (2013), these fringes originate mainly from the shape error of the substrate which is transferred to the conformal multilayer coating. To investigate this
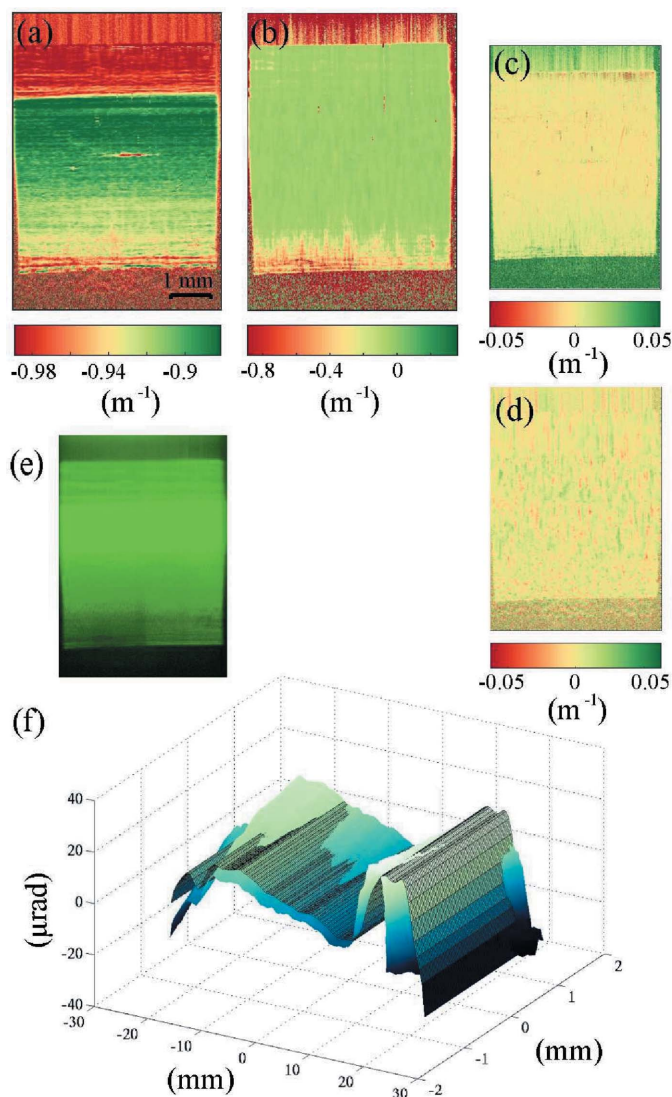
Figure 6
Curvature fields (a) $\partial^2 W/\partial x^2$, (b) $\partial^2 W/\partial y^2$, (c) $\partial^2 W/\partial x \partial y$ and (d) $\partial^2 W/\partial y \partial x$. (e) First (single) raw image of the 2D mesh scan of the speckle generator. The beam passes through the speckle generator and is reflected on the mirror before impinging on the detector. (f) 3D rendering of the mirror's tangential slope error. The darker surface shows the slope error obtained with the ESRF Long Trace Profilometer.

effect, two measurments were performed. First, an uncoated mirror was illuminated under total external reflection, and later another high-quality substrate after coating at the multilayer Bragg angle. The XSS method was applied in one dimension to benefit from its higher angular sensitivity and high resolution. We thus present results from (i) a 90 mm long silica substrate polished at the Institut d'Optique Graduate School and (ii) a sample coated with a multilayer at the ESRF with the following deposition characteristics: $[\text{W}/\text{B}_4\text{C}]_{60}$ and $d = 4$ nm.

The speckle generator was placed, as in the previous experiment, at a distance of 400 mm upstream of the mirror, while the distances from the X-ray optics to the detector were $d = 915$ and 955 mm for the respective measurements. The grazing-incidence angle of the photons on the mirror was $0.21°$

and the working energies were $E = 8$ keV for the uncoated substrate and $E = 17$ keV for the multilayer coating. The detector used was the PCO Edge 4.2 camera coupled with optics giving a pixel size of 0.63 µm. The scan of the speckle generator consisted of 150 points of different vertically aligned positions with a step size of 0.25 µm.

Fig. 7(d) shows a good correlation between the observed intensity modulation and the measured mirror curvature for the uncoated substrate. On the same graph, one can observe that the corresponding problematic height error amplitude is of the order of the wavelength, i.e. at the ångström level. In the right-hand part of Figs. 7 [panels (f)–(g)], the correlation between the intensity modulation and the local wavefront curvature is even more striking, while the corresponding peak-to-valley defects in the medium spatial wavelength are smaller than an ångström. This range of height error is inaccessible with current offline metrology, and currently available technology and techniques do not allow for the correction of such small defects.

Fresnel–Kirchhoff numerical propagators currently permit the accurate prediction of the intensity produced by optics with known errors, but ongoing work on the inverse problem should help us define clear specifications for the mirror design in terms of spatial spectral power. As a matter of fact, one can prove a relationship linking the intensity modulations to the mirror curvatures in the mm^{-1} spatial frequency. Eventually, such mirror curvature corresponds to the height of the mirror defects with an amplitude of the order of the wavelength. The experimental demonstration of this relationship supports the theoretical model published by Nicolas & García (2013), which explains the intensity modulation in term of surface curvature error. Older models with visible light (Berry, 2006) and whose analytical solutions can be easily applied to the X-ray regime are also consistent with the present observations.

3.2.3. Adaptive optics optimization. Here we apply the speckle scanning methods to X-ray adaptive optics optimization, which is relevant, for instance, in achieving smaller focal spots by actively reducing the optical aberration (Matsuyama et al., 2016). Although a first demonstration was described by Berujon (2013) where both XST and XSS were combined, further work has highlighted the advantages of the XSS technique for online X-ray optics optimization due to its high angular sensitivity.

The most frequently used type of X-ray adaptive optics are deformable mirrors with controllable surfaces. These optics can be either of the bimorph kind, with a small or a large number of piezo actuators, or they can be mechanical benders that use motors with incremental steps in the nanometre or sub-nanometre range. Whilst bimorph mirrors usually offer a larger degree of freedom due to the use of more actuators, they also require electronics with high stability to keep the actuators steady over long periods of time, which is not the case with dynamically bent mirrors.

The BM05 beamline of the ESRF is equipped with a Kirkpatrick–Baez reflective optics system composed of two mechanically bendable mirrors mounted orthogonally. Each mirror bender has two encoded actuators at the ends of the
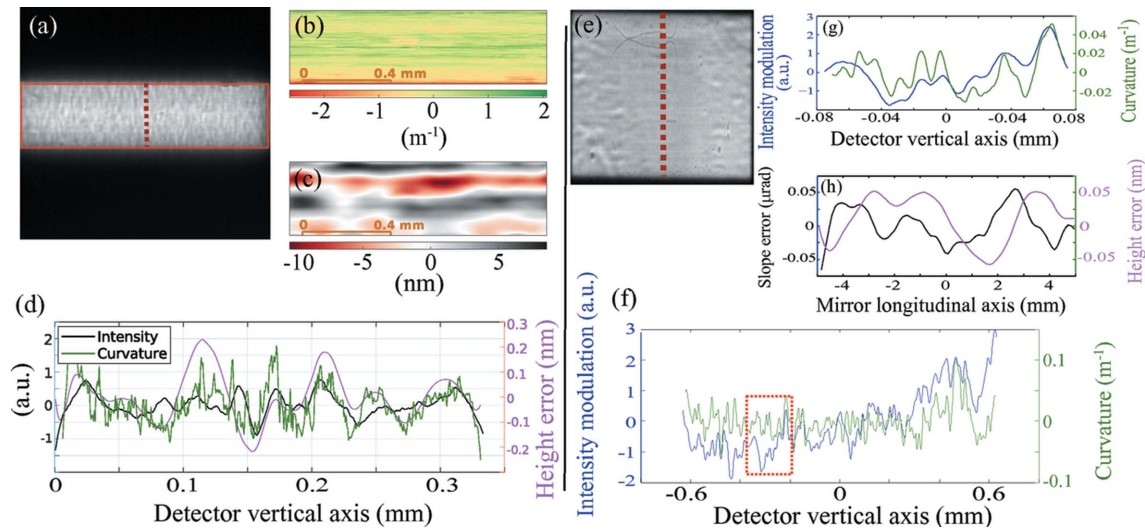
Figure 7
(Left) Flat substrate metrology and (right) multilayer metrology. For the flat substrate: (*a*) First raw image of the speckle generator upon total external reflection on the mirror. (*b*), (*c*) Measured tangential curvature of the mirror, light being reflected in the vertical direction and falling onto the square marked in panel (*a*); corresponding tangential (*b*) slope error and (*c*) height error. (*d*) Intensity (black line), curvature (purple line) and height profile (pink line) measured across the mirror along the dashed line in (*a*). For the multilayer coated mirror: (*e*) First raw image of the speckle generator upon reflection on the mirror surface. (*f*) The intensity modulation across the reflected beam marked by the dashed line in (*e*) is plotted in blue and the curvature measured for this same profile is plotted in green. (*g*) Enlargement of the region marked by the red square in (*f*) after the removal of a polynomial of order two. (*h*) Slope and height profiles corresponding to the curvature of (*g*).

mirror surface. For metrology, this system permits the evaluation of various schemes for optics optimization and the exploration of the potential of the methods.

The setup of this experiment is shown in Fig. 8, with the speckle generator located downstream of the reflective optics. Placing the speckle generator after the adaptive optics is important since we want to optimize the ensemble of all the optical components present along the beamline, hence they have to be upstream of the speckle generator. What matters here is the final state of the beam phase, adding the contribution of all the beamline optics.

A good explanation of the theory of wavefront optimization through matrix inversion and of the possible processing schemes is given by Tyson (2010*a*). In short, wavefront optimization through matrix inversion consists of a first phase of measuring, for each of the actuators, the effect of an incremental step on the wavefront or its derivatives. Hence,

Figure 8
The configuration for focusing of the KB bender.

differential metrology is required for this task. It can be done either by working in a differential mode as described earlier, or by using the accurate and easy to implement XSS self-correlation mode, as is the case here. This consists of subtracting the wavefront measured before and after having applied a command to an actuator. The response function of each actuator is then placed as a column of a matrix **A** with as many columns as the number of degrees of freedom (actuators) that the system contains. This process implies that the system is repeatable and even linear, which often calls for encoders to guarantee the correct displacement of each actuator.

Then, using the notation Υ for the vector wavefront error (or for its gradient or curvature) as measured with absolute metrology, and Ψ for the piezo correction that needs to be applied, the problem requires solution of the linear equation $\Upsilon + \mathbf{A}\Psi = 0$. This equation is usually solved in the least-squares sense by matrix inversion to obtain $\Psi = -\mathbf{A}^{-1}\Upsilon$. Because the matrix **A** is not square and singular with computer working precision, the inversion is operated in the Moore–Penrose pseudo-inverse sense using singular value decomposition, Gauss elimination, Cholesky decomposition or any other alternative numerical method (Barnett, 1990).

The optimization of the wavefront can be done on the wavefront surface, on its gradient or on the curvature, all three being linked by an integral relation. Usually, this question can be answered by the nature of the deformation created by the actuators: bimorph mirrors combine well with curvature-sensing systems, while benders provide better results when used in combination with slope measurements (Tyson, 2010*a*). Regarding the fitting of polynomials to the wavefront error, one can also fit the derivative of the surface polynomial to the

Sebastien Berujon *et al.* · Beam characterization using random modulation: practice
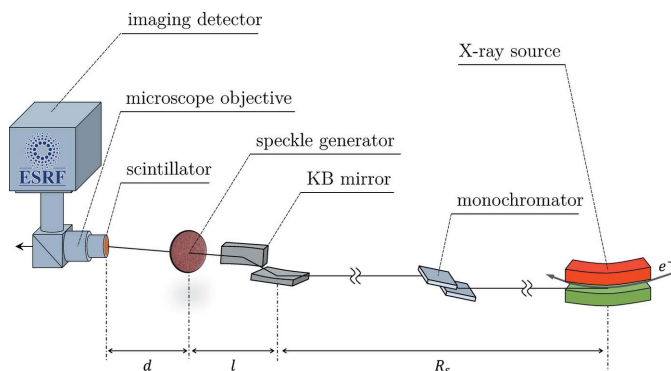
slope error to infer the wavefront error directly in a modal manner. Even so, in the X-ray regime the zonal approach can be favoured since the resolutions used are high with respect to what is encountered in visible light optics. Such a zonal approach permits a full description of the system, although only the low orders can be compensated.

Fig. 9 shows the actuator influence function on (c) the wavefront, (b) the wavefront slope and (a) the wavefront curvature of the two actuators of the BM05 vertical focusing bender, measured 240 mm from the mirror focus (which for this case was also set to approximately one focal distance of the mirror for convenience). Note that the tilt has been removed by subtracting the mean value of the slope. Figs. 9(d)–9(f) show the wavefront errors, the wavefront gradient errors and curvature errors, respectively, after three correcting iterations. One can observe that the method converges quickly thanks to the high accuracy of the online metrology, while the limited number of actuators in the system is the main limitation on the system's performance. Indeed, the S shape of the remaining wavefront error, corresponding to a polynomial of order three, indicates that more than two actuators would be needed to correct the optics further. Additional work on
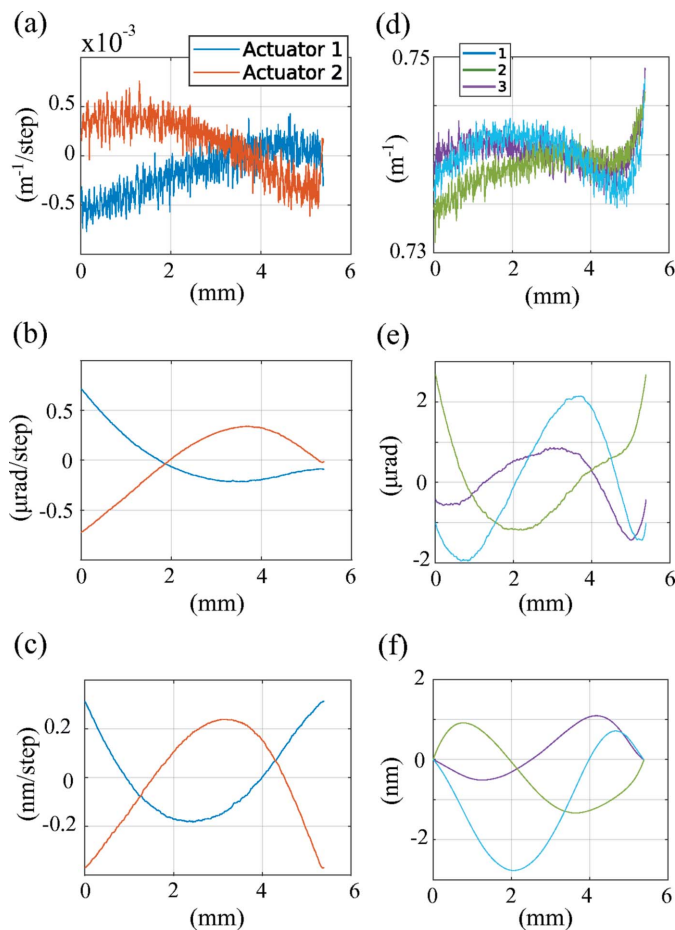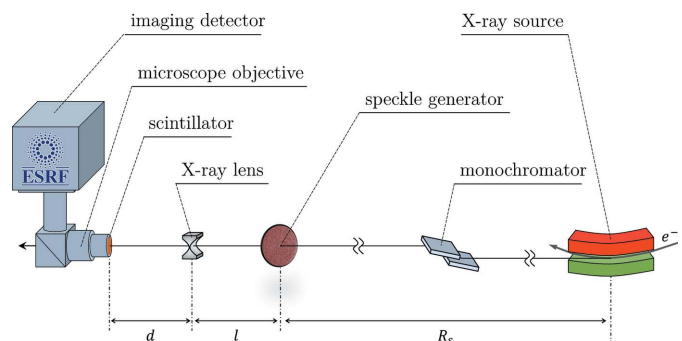
bimorph mirrors with more actuators proved the validity of the concept for higher-order systems (Berujon, 2013).

3.3. Refractive optics

3.3.1. Single compound refractive lens. Another interesting application of X-ray speckle-based metrology is the characterization of inline refractive optics, especially to assess the shape errors of lenses prior to permanent installation on a beamline.

For such at-wavelength characterization, we use the setup sketched in Fig. 10, where the speckle generator, the optical component and the detector are all aligned. XST, XSVT, XSS or any more advanced scheme can be employed here to recover the phase shift induced by an overall weakly (single-lens) refractive optics. We choose to implement the XSVT technique for routine lens characterization at the ESRF, due to the following points:

(i) We want to keep the setup simple for such characterizations and the probe beam is to be left with its original collimation (no additional focusing or beam-shaping optics are used). The lateral resolution of XSVT is the detector resolution, which is higher than that obtained using the XST technique (averaging over pixel groups). Besides, the XSVT resolution equals that achieved with the other remaining schemes, although the latter do not provide additional sensitivity benefits when using an almost-collimated probe beam.

(ii) The angular dynamic range of the XSVT technique is theoretically not limited as is the case for XSS, where the size of the speckle generator mesh scans sets the maximum displacement vector and hence the phase gradient. This aspect is of value when measuring a series of lenses with varying design parameters.

(iii) The number of necessary images for using XSVT properly is of the order of $2N$ images taken at random positions of the speckle generator, while it is of the order of M^2 images for XSS and hybrid schemes (M being the number of lateral points in the membrane position mesh and typically in the range [11; 31]). In the following case we use $N = 81$ images in each scan with the speckle generator located at 81 positions on a $\log_2$ grid. The reference data set can be reused for several lens measurements. At the ESRF, lenses are often measured in batches of ten, which corresponds to the collection of 891

Figure 9
Influence function of the actuators on the wavefront (a) curvature, (b) slope and (c) height as a function of the detector's vertical axis. Errors on the wavefront (a) curvature, (b) slope and (c) height as a function of the detector's vertical axis after the (d) first, (e) second and (f) third corrections.

Figure 10
The setup for refractive optics characterizations.

images, or 972 when using two different reference data sets to evaluate and compensate for eventual beam drift and fluctuations of the beamline.

Here and in Section 3.3.3 we apply the technique in differential mode. This means that two stacks of images are used to analyse each lens, one with the lens present in the beam and a reference data set acquired without the lens. Using the differential mode permits the isolatation of the contribution of the investigated optics (the lens) on the X-ray beam phase, putting aside the errors coming from the upstream optics.

Fig. 11 shows the information retrieved for an aluminium lens using the XSVT technique from two stacks of images. The lens was produced in a first batch of Al lenses at the ESRF with a design radius at the apex of $R_{apex} = 50\,\mu m$ and a physical aperture of $\sim440\,\mu m$. The speckle generator was made of cellulose acetate with a 1.2 μm pore size. The distance from the speckle generator to the lens was 400 mm and the distance from the lens to the detector was $d = 905$ mm. The detector was a PCO Edge 4.2 camera coupled to a $10\times$ microscope objective. From the undistortion step of the images, the effective pixel size of the system was calculated as $p_{ix} = 0.63\,\mu m$. All 2D maps shown in Fig. 11 have been corrected for detector distortion. The photon energy was $E = 17$ keV.

The differential wavefront gradients induced by the lens [Figs. 11(a) and 11(b)] were computed using the XSVT correlation equation presented in the theoretical paper. The wavefront gradient errors were calculated by removing the best vertical (or, respectively, horizontal) plane fit from the wavefront gradients. The wavefront error W_{err} of the lens was obtained by integration of the wavefront gradient errors, and finally the thickness error T_{err} was found by the linear relation $T_{err} = W_{err}/\delta(\lambda)$. For the case presented here, $\delta_{Al}(17\,keV) = 1.87 \times 10^{-6}$.

Assuming the wavefront to be the sum of a perfect spherical surface W_s and an error deviation from it W_{err}, we can calculate a differential focusing distance f along an axis $\hat{\mathbf{r}} = \mathbf{r}/|\mathbf{r}|$ from a 2D fit of the surface derivative of $W = W_s + W_{err}$:

$$f = \left\langle \frac{\partial^2 W}{\partial \hat{\mathbf{r}}^2} \right\rangle = \left\langle \frac{\partial^2 W_s}{\partial \hat{\mathbf{r}}^2} \right\rangle, \quad (3)$$

where $\langle \ldots \rangle$ denotes the quadratic mean and by definition we have $\langle W_{err} \rangle = 0$. Note that, for a perfectly rotationally symmetrical lens, f is constant for any $\mathbf{r}$. Experimentally, however, this is often not the case, with most lenses presenting some degree of astigmatism.

The calculation of f permits the determination of the radius of a single biconcave lens at the apex, which is equal to

$$R = 2f\delta(\lambda). \quad (4)$$

For the lenses presented, one can observe in Figs. 11(c)–11(e) rings which are attributed to imperfections in the machining of the punches that have been used during the lens fabrication process.

This XSVT method is now routinely applied at the ESRF for the inspection of newly acquired or manufactured lenses.
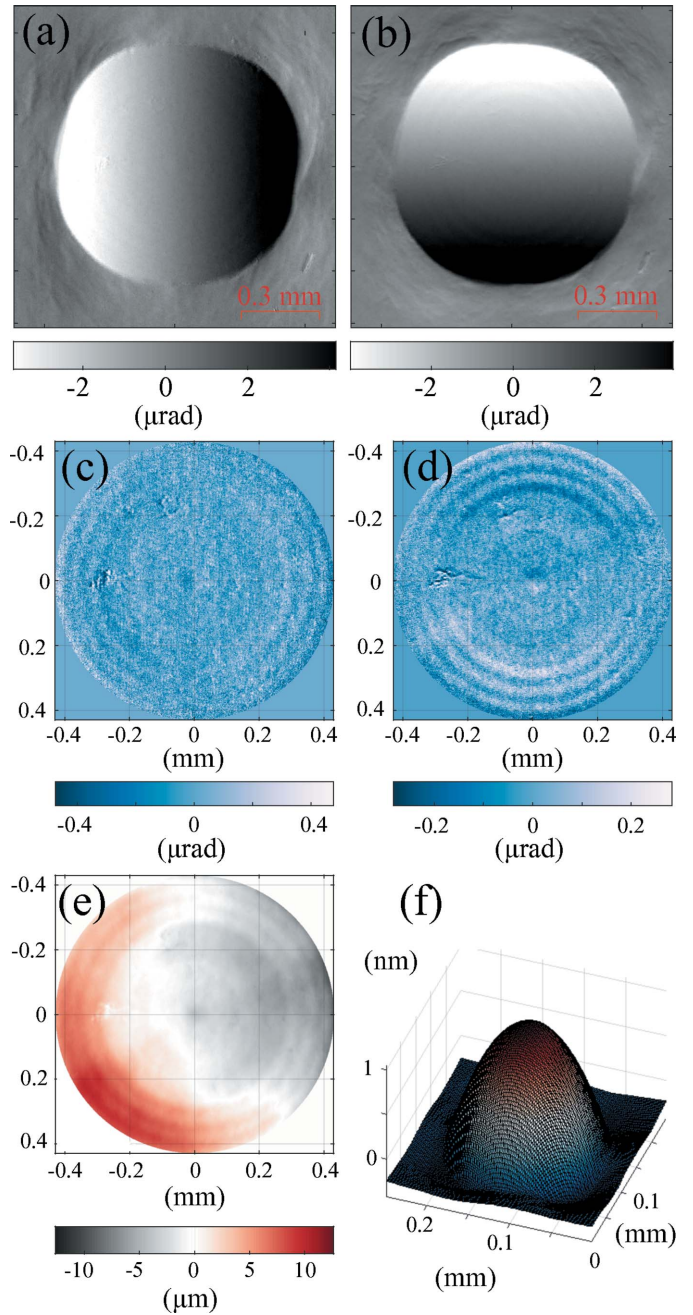
Figure 11
(a) Horizontal and (b) vertical wavefront gradients. (c) Horizontal and (d) vertical wavefront gradient errors. (e) Projected shape error recovered from (f) the measured wavefront.

With only a few minutes necessary for the characterization of a lens, the very sensitive method is easy to implement for batch analysis. Stacks of lenses are also studied following the same methodology, usually with a higher energy selected. This allows the detector to intercept a beam that is still large enough (at lower energies the focusing would reduce the beam size at the detector) and thus provides an acceptable resolution.

This type of metrology data represents what is called a zonal approach, i.e. 2D pixellated maps of the optics aberrations.

From these, a modal decomposition can be obtained (Tyson, 2010b). Indeed, an easy and fast way of representing a lens-shape error consists of decomposing its resulting aberrated wavefront onto orthonormal polynomials (Mahajan & Dai, 2007). This description permits a more rapid interpretation of the types of defect in the lens and allows a comparison with other optics, as is routinely done for visible light optics.

3.3.2. Strongly refracting optics. The previously studied Al single lens is weakly focusing, as is the case for most refractive optics in the X-ray regime (Roth *et al.*, 2017), although some X-ray refractive optics consist of several elements printed or made from a single bulk, which cannot be dismantled into elementary parts, thus presenting a much stronger focusing effect.

When the focusing effect is very strong and/or when the induced phase distortion varies rapidly across the aperture, the implementation of a speckle technique in the differential mode, as done in the previous section, can become difficult or even impossible. Indeed, with a very large and spatially rapidly varying distortion of the wavefront, the correlation algorithm can no longer track the modulation pattern from one stack of images to the other. In that case, the absolute mode can become efficient under the hypothesis that the phase defects present in the incoming beam are much smaller than those generated by the optics under investigation. For a beamline such as BM05, where only two beryllium windows and two flat crystals interact with the beam (with no other focusing optics), this assumption is often valid.

The XSS self-correlation mode (see Section 2.2.5 of the theoretical paper) can be employed in the same way as for the online characterization of the mirror in Sections 3.2.1 and 3.2.2. Fig. 12 illustrates the method on an SU-8 lens stack consisting of two crossed 1D lens stacks produced by X-ray LIGA.

The focal length of this lens, comprising 65 vertically aligned lenslets and 65 horizontally aligned lenslets, at the measurement energy of $E = 30$ keV, was 250 mm. Note that the speckle generator was mounted after the lens, at a distance $l = 95$ mm. This location of the speckle generator overcomes the problems encountered when the lens material scatters too strongly, thus blurring or masking the random modulation pattern. The detector was located at $d = 405$ mm from the speckle generator or $d = 2f$. At this position, the magnification of the random speckle pattern is equal to about -1. The speckle generator was scanned twice (2×100 images), once in each transverse direction of the beam, with a step size of 1 μm. As in Section 3.2.1, the wavefront gradient errors were recovered from integration of the curvature maps obtained by the XSS technique where $\kappa = (1 - v/\Delta\mathbf{r})/d$ [see Berujon *et al.* (2020)]. Displacement vectors were calculated from pixels located at a distance of $\Delta\mathbf{r} = 4p_{\text{ix}}$. Fig. 12 shows that this lens stack suffers from significant wavefront gradient errors of the order of a few microradians. This is about 30 to 40 times higher than seen for the single Al lens in Fig. 11. However, here we have a stack of 2×65 lenses, which means that the error on an individual lens basis is of the same order of magnitude, if not smaller.
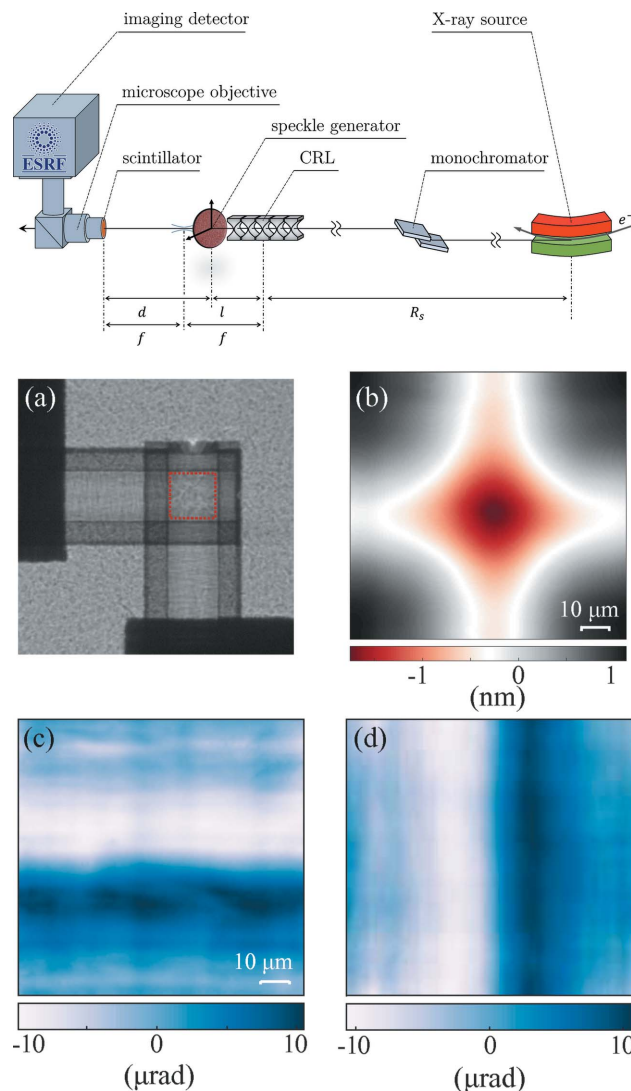
Figure 12
(Top) The setup for the analysis of a strongly focusing lens stack. (*a*) The first image of the stack, showing the crossed lenses with the overlying randomly modulated wavefront. (*b*) The calculated wavefront error for the area marked with the red line in (*a*). (*c*) Vertical and (*d*) horizontal wavefront gradient errors of the same area.

3.3.3. Monochromaticity requirements. The lens analysis examples shown above were obtained under monochromatic conditions with an energy selectivity corresponding to $\Delta E/E \simeq 10^{-4}$. For a quick comparative study, a diamond lens known for having noticeable aberrations was measured under similar conditions but with two different bandwidths, of $\Delta E/E \simeq 10^{-4}$ as before and $\Delta E/E \simeq 10^{-2}$ using a multilayer monochromator. In both cases, the mean photon energy was $E = 15$ keV.

The lens was characterized in both cases using the XSVT technique, with 49 scanning points [*cf.* Section 2.2.3 in the paper by Berujon *et al.* (2020)] to recover the wavefront gradient and shape. The comparative results presented in Fig. 13 show that these results are in very good agreement despite a spectral bandwidth ratio of ~70. The optical aberrations of the lens shown in Figs. 13(*c*)–13(*d*) and 13(*g*)–13(*h*)
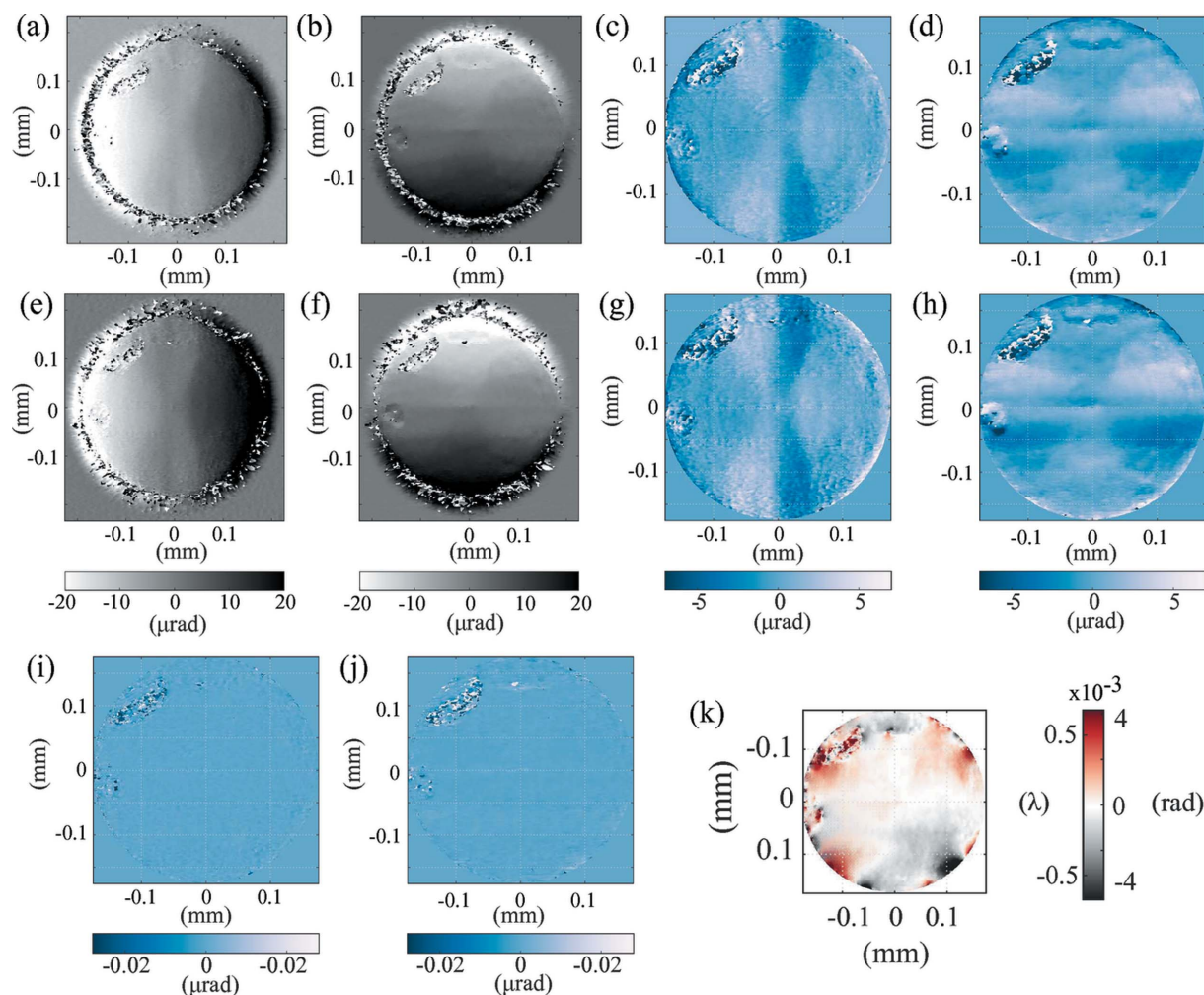
Figure 13
Diamond lens prototype characterization. (a) Horizontal and (b) vertical differential wavefront gradients measured using a double-crystal monochromator and (c), (d) the associated wavefront gradient error. (e)–(h) Equivalent measurements obtained using a multilayer monochromator. (i), (j) The difference maps of (i) the horizontal gradients and (j) the vertical gradients. (k) The difference phase map calculated using (i) and (j).

match very well down to the sub-microradian scale. This can be more precisely observed in the wavefront gradient difference maps shown in Figs. 13(i)–13(j). There, the gradient differences are homogeneous and in the range of tens of nanoradians, except at points where the correlation was poor due to a lack of light. Finally, the difference phase map shown in Fig. 13(k), calculated from the maps in Figs. 13(i)–13(j), confirms the good agreement between the two measurements, with a wavefront difference between them of less than 0.001 of a wavelength.

This experiment quantitatively confirms that, in the near-field, requirements on longitudinal monochromaticity are not stringent. Whilst a bandwidth of a couple of percent is still very selective with respect to a laboratory source, numerical simulations showed that, by working with a broader source spectrum and introducing the concept of equivalent energy, quantitative results were still achievable (Zdora *et al.*, 2015). However, for quantitative metrology, the refractive index of the material $\delta(\lambda_{eq})$ must be selected carefully in order to recover the material's thickness.

4. Conclusions

Several examples employing X-ray speckle-based methods for the characterization of X-ray optics have been presented, illustrating the potential of this approach in a variety of situations. The applicability of X-ray speckle methods has been demonstrated with a low-coherence source. This suggests that the presented schemes could possibly be applicable to laboratory sources, provided a few adjustments are implemented, especially in term of beam monochromaticity. These at-wavelength characterization methods are now routinely available at synchrotrons as illustrated in this paper. They may also become attractive for the XFEL sources that have recently started operation. Speckle-based methods should thus help in the manufacture of better optics during their production stage or, for instance, enable the manufacture of compensating optics.

Finally, while the present paper reviews some fundamental concepts in using speckle-based methods for adaptive optics, we believe that the XSS method in particular allows us to

achieve the ultimate optimization and focusing of X-rays with actuator optics and will be helpful on beamlines to achieve, easily and routinely, the optimal alignment of nanobeam optics.

References

Arnison, M. R., Larkin, K. G., Sheppard, C. J. R., Smith, N. I. & Cogswell, C. J. (2004). *J. Microsc.* **214**, 7–12.

Barnett, S. (1990). *Matrices: Methods and Applications. Oxford Applied Mathematics and Computing Science Series.* Oxford: Clarendon Press.

Berry, M. V. (2006). *Eur. J. Phys.* **27**, 109–118.

Berto, P., Rigneault, H. & Guillon, M. (2017). *Opt. Lett.* **42**, 5117–5120.

Berujon, S. (2013). *At-Wavelength Metrology of Hard X-ray Synchrotron Beams and Optics.* PhD thesis, ESRF, Grenoble, France (http://www.theses.fr/en/2013GRENY010).

Berujon, S., Cojocaru, R., Piault, P., Celestre, R., Roth, T., Barrett, R. & Ziegler, E. (2020). *J. Synchrotron Rad.* **27**, 284–292.

Berujon, S., Wang, H., Alcock, S. & Sawhney, K. (2014). *Opt. Express*, **22**, 6438–6446.

Berujon, S., Wang, H. & Sawhney, K. (2012a). *Phys. Rev. A*, **86**, 063813.

Berujon, S. & Ziegler, E. (2012a). *Opt. Lett.* **37**, 4464–4466.

Berujon, S. & Ziegler, E. (2012b). *Opt. Lett.* **37**, 4464–4466.

Berujon, S. & Ziegler, E. (2015). *Phys. Rev. A*, **92**, 013837.

Bérujon, S., Ziegler, E., Cerbino, R. & Peverini, L. (2012b). *Phys. Rev. Lett.* **108**, 158102.

Berujon, S., Ziegler, E. & Cloetens, P. (2015). *J. Synchrotron Rad.* **22**, 886–894.

Frankot, R. T. & Chellappa, R. (1988). *IEEE Trans. Pattern Anal. Machine Intell.* **10**, 439–451.

Inoue, T., Matsuyama, S., Kawai, S., Yumoto, H., Inubushi, Y., Osaka, T., Inoue, I., Koyama, T., Tono, K., Ohashi, H., Yabashi, M., Ishikawa, T. & Yamauchi, K. (2018). *Rev. Sci. Instrum.* **89**, 043106.

Mahajan, V. N. & Dai, G. (2007). *J. Opt. Soc. Am. A*, **24**, 2994–3016.

Matsuyama, S., Nakamori, H., Goto, T., Kimura, T., Khakurel, K. P., Kohmura, Y., Sano, Y., Yabashi, M., Ishikawa, T., Nishino, Y. & Yamauchi, K. (2016). *Sci. Rep.* **6**, 24801.

Morawe, C., Barrett, R., Friedrich, K., Klünder, R. & Vivo, A. (2013). *J. Phys. Conf. Ser.* **425**, 052027.

Nicolas, J. & García, G. (2013). *Proc. SPIE*, **8848**, 884810.

Noll, R. J. (1978). *J. Opt. Soc. Am.* **68**, 139–140.

Roth, T., Alianelli, L., Lengeler, D., Snigirev, A. & Seiboth, F. (2017). *MRS Bull.* **42**, 430–436.

Southwell, W. H. (1980). *J. Opt. Soc. Am.* **70**, 998–1006.

Tyson, R. K. (2010a). *Principles of Adaptive Optics*, 3rd ed., ch. 6, *Series in Optics and Optoelectronics.* Boca Raton: CRC Press.

Tyson, R. K. (2010b). *Principles of Adaptive Optics*, 3rd ed., ch. 5, *Series in Optics and Optoelectronics.* Boca Raton: CRC Press.

Wang, H., Kashyap, Y., Laundy, D. & Sawhney, K. (2015). *J. Synchrotron Rad.* **22**, 925–929.

Zdora, M.-C., Thibault, P., Pfeiffer, F. & Zanette, I. (2015). *J. Appl. Phys.* **118**, 113105.

Ziegler, E., Hoszowska, J., Bigault, T., Peverini, L., Massonnat, J. Y. & Hustache, R. (2004). *AIP Conf. Proc.* **705**, 436–439.